Supplement: Tabletop EUV reflection dual-polarisation ptychography enables high-throughput nanoscale material-mapping and angstrom-scale profilometry

This supplementary material provides additional details for the experiments described in the main manuscript. Starting with the implementation of structured illumination in reflection geometry in Section 1. Next, Section 2, describes the required frequency interpolation of intensities [1] before ptychographic reconstruction and the object-to-detector calibration via the purity search [2]. Section 3 illustrates the complex-valued reconstructions of the HDR datasets. For each dataset, we report: acquisition parameters, experimental times, reconstruction hyperparameters, and quantitative evaluation of their spatial resolution via Fourier ring correlations and the 1/2-bit criteria [3]. Section 4 summarizes the achieved throughput. Section 5 showcases locally distinct material responses. Section 6 illustrates the optical phase difference in a reflection geometry. Section 7 evaluates the standard phase error over different FOVs, and finally Section 8 list the material parameters used for the reflectivity plots in the main manuscript.

1. STRUCTURED ILLUMINATION IN REFLECTION GEOMETRY

Implementing an amplitude mask for tailoring the illuminating wavefront in reflection geometry imposes an additional constraint: it must be placed close to the sample to create a confined probe, yet it must not block the reflected beam on its way to the detector. To satisfy both requirements, we use a mask with two apertures: one patterned opening that structures the incident beam, and a second, larger opening that allows the reflected signal to pass towards the detector without obstruction. Fig. S1 illustrates this geometry.

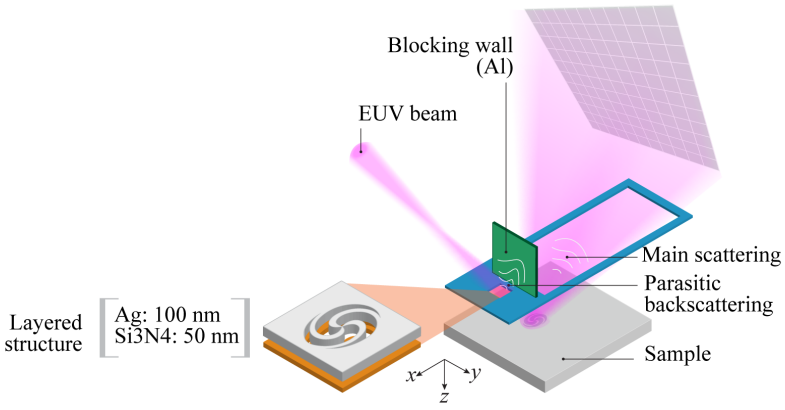

Fig. S1. Structured illumination mask and collection geometry. (*left*) Schematic of the amplitude mask, showing the patterned spiral aperture that structures the incident EUV beam and its layered structure. (*right*) Adjacent, larger collection aperture for the reflected beam. A thin blocking wall (green) is integrated into the mask holder at the boundary between the two apertures to block back-scattered signal from the opaque regions of the mask while preserving the desired collection numerical aperture.

The patterned spiral mask is fabricated on a 50 nm Si_3N_4 membrane by first depositing $\sim$ 100 nm of Ag and then FIB milling the spiral structure. The coating was chosen to maximise the amplitude suppression of the transmitted field in the opaque regions and thus increase the modulation contrast of the structured probe. However, the required suppression introduces a

practical caveat: photons that do not pass through the patterned aperture can be reflected from the mask surface towards the detector. Without further measures, our measurements would therefore contain two superimposed signals, one from the sample and an unwanted contribution from mask back-scattering. To suppress this parasitic signal, we integrate a thin blocking wall into the mask holder at the edge between the structured illumination aperture and the collection aperture (Fig. S1). With a thickness of $\sim$ 400 µm, the wall is sufficiently thick to absorb the EUV radiation originating from the mask, yet sufficiently narrow to avoid clipping the collection numerical aperture.

2. INTERPOLATION OF NON-COPLANAR INTENSITIES AND Z-CALIBRATION

In a ptychographic pipeline, the reconstruction algorithm alternates between the object domain (real space) and the detector domain, which we interpret as the Fourier (reciprocal) space of the object. Propagation between these domains relies on fast Fourier transforms (FFTs), which assume that the recorded intensities are sampled on a regular Cartesian grid in spatial-frequency space. In practice, however, the equally spaced pixels on the detector do not necessarily correspond to a regularly spaced grid in reciprocal space, so an interpolation step of the measured diffraction intensities is required to satisfy the FFT sampling requirements.

Such a sampling mismatch arises in both transmission and reflection geometries. In transmission, at sufficiently large numerical apertures [4] (e.g. NA $\approx$ 0.5), spatial frequencies near the detector edges become compressed relative to the centre [Fig. S2(a)], because the detector samples points on a curved Ewald sphere rather than on a plane. In reflection geometry, for example at a 45° angle of incidence, the same high-NA effect is present, but even at more moderate numerical apertures (e.g. NA $\approx$ 0.25 in our case) the dominant distortion arises from the non-coplanar arrangement of the sample and detector planes [1], which produces a non-uniform mapping of detector pixels into reciprocal space [Fig. S2(b)]. Panels (c) and (d) in Fig. S2 show example diffraction patterns from our measurements before and after interpolation onto a regular frequency grid, respectively. Together, they illustrate both the distorted sampling and its correction; the dashed lines highlight the distorted mapping.

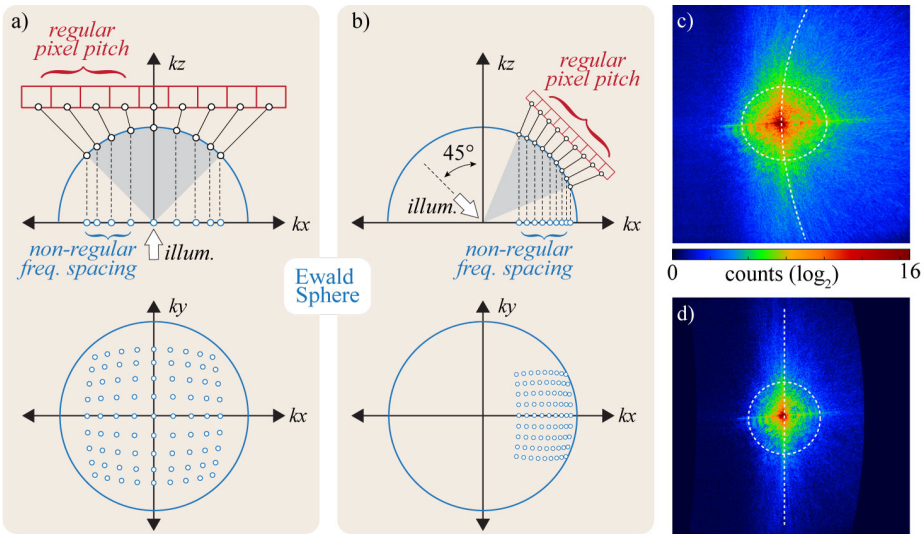

Fig. S2. Ewald-sphere sampling and tilted-plane correction for EUV reflection ptychography. (*a*) Example of the sampling distortion in a transmission geometry for NA $\approx$ 0.5, where the equally spaced detector pixels are mapped to a non-uniform sampling in spatial-frequency space. (*b*) Corresponding sampling distortion in a non-coplanar reflection geometry at a 45° angle of incidence, where the tilt between the sample and detector planes leads to a non-uniform mapping of the spatial-frequency space. (*c*) Measured diffraction pattern on the detector, showing the distorted sampling. (*d*) Same diffraction data after tilted-plane correction, restoring uniform sampling. Dashed lines in panels (d) and (e) highlight the distorted mapping and its correction.

In principle, one could avoid this interpolation step by using a propagation operator that

explicitly accounts for the curved Ewald sphere and the tilted, non-coplanar detector geometry. In practice, a propagator that handles this geometry with adjustable object-plane sampling while remaining computationally efficient is not yet widely available in standard ptychographic toolboxes, so we adopt the interpolation-based approach here.

Each background-corrected diffraction dataset is interpolated onto a regular reciprocal-space grid as described above. In addition, during reconstruction we do not enforce zero intensity outside the interpolated Ewald patch in reciprocal space. Only this interpolated region is constrained by the measured data; the remaining Fourier pixels are left unconstrained, in analogy with missing-data formulations used in super-resolution ptychography [5]. We use the open-source code *PtyLab* [6] for ptychographic reconstruction. In particular, we employ the gradient-based iterative mPIE engine [7] with a mixed-state probe model (with four modes) [8] and an additional background estimation [9] to account for partial spatial coherence of the source and residual background noise. Although the EUV radiation is generated from a coherent laser, small fluctuations in the driving laser and mechanical vibrations on the order of a few tens of nanometres from neighbouring equipment can degrade the measured speckle patterns and reduce reconstruction quality.

We quantify the degree of partial coherence captured by the mixed-state model using the purity metric μ [10], for which the effective number of modes is given by $M_{\text{eff}} \approx 1/\mu^2$. For our data, the reconstructed probe has a purity of $\mu \approx 0.67$, corresponding to $M_{\text{eff}} \approx 2.2$, i.e. an effective coherence rank of about two to three modes. This confirms that a four-mode probe model is mildly overcomplete, provides a safety margin against residual instabilities and modelling errors, and avoids heavy over-parameterisation of the reconstruction.

To improve the reconstruction quality further, we refine the sample–detector distance by maximising this purity metric [11]. For each candidate distance z, we perform a reconstruction and evaluate μ. The calibrated distance z_{opt} is taken as the value that maximises μ. The calibrated z_{opt} is then used to re-interpolate the background corrected data, and a second purity scan is performed to confirm convergence of z_{opt}. Fig. S3 shows the purity metric as a function of z over the scanned range, together with the four reconstructed illumination modes and their relative energy content. This calibration is repeated after each sample is installed, as small offsets can be introduced when repositioning the stages.

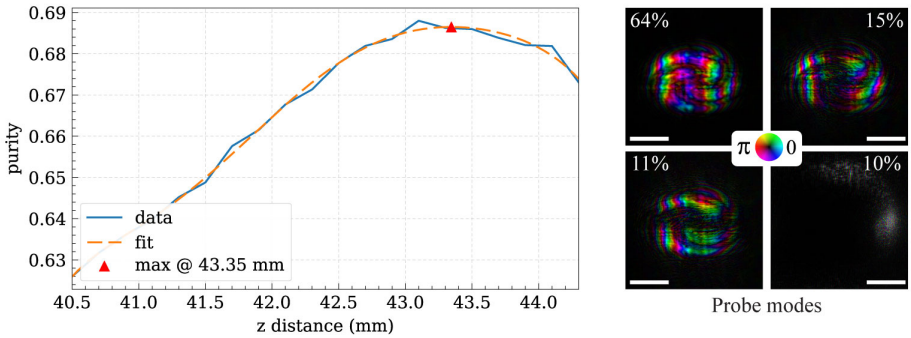

Fig. S3. Calibration of the sample–detector distance using the mixed-state purity metric. (*left*) Purity metric μ as a function of trial distance z; the optimal distance is chosen at the maximum of μ. (*right*) Reconstructed illumination modes corresponding to the optimal distance, together with their relative energy fractions, illustrating the partial spatial coherence captured by the four-mode model. Scalebar is 10 µm.

3. OVERVIEW OF COMPLEX RECONSTRUCTED DATASETS

Here, we summarize the reconstructed results for the HDR datasets, including the reconstructed illumination and its energy content.

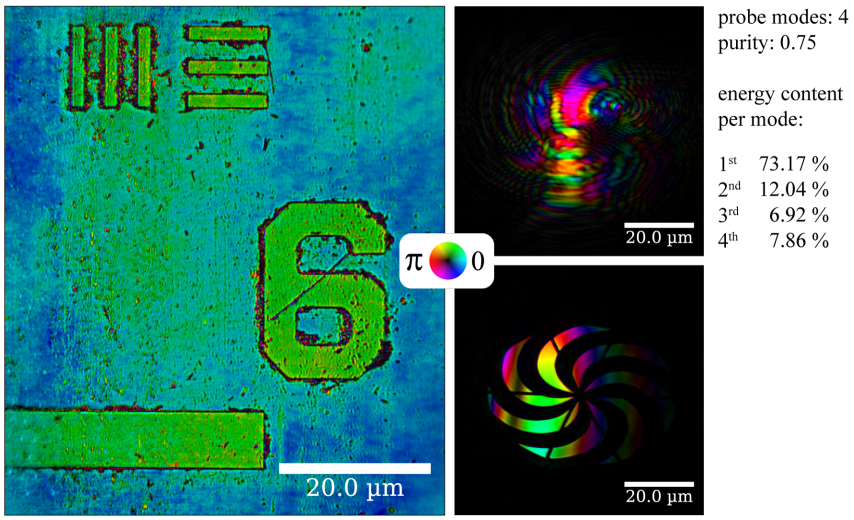

Fig. S4. Complex-valued reconstructions of the USAF datasets; hue encodes phase, brightness encodes amplitude. (a) Reconstructed sample. (b) Reconstructed probe (first mode) and its backpropagated field to the mask plane (c). The values for the obtained probe purity and the energy content of each mode are listed.

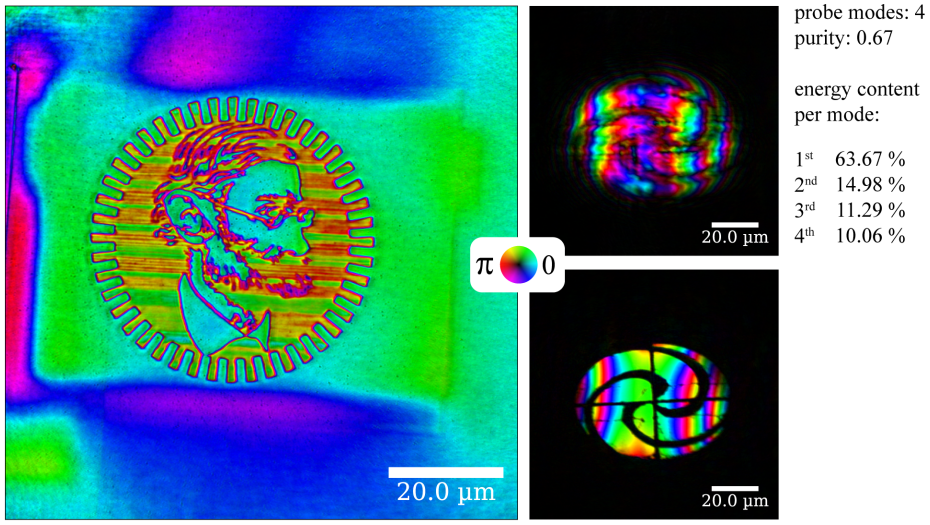

Fig. S5. Complex-valued reconstructions of the Abbe portrait HDR datasets; hue encodes phase, brightness encodes amplitude. (a) Reconstructed sample. (b) Reconstructed probe (first mode) and its backpropagated field to the mask plane (c). The values for the obtained probe purity and the energy content of each mode are listed.

A. USAF test target

(a) Acquisition parameters	
Number of scan positions	497
Average step size	3.4 μm
Distance to detector z	43.44 mm
Wavelength	46.5 nm
Angle of incidence θ_i	45 °
Detector pixel size Δ_q	22 μm
Detector size N_q	1024×1024

(b) Timing breakdown (per position and total)	
Avg. dwell time per position	300 ms
Avg. readout time per frame	150 ms
Avg. saving time per position	40 ms
Exposure time per position	100 ms + 2 s
Total exposure time	1044 s
Total acquisition time	**∼22 min**

Table S1. Overview of acquisition parameters and timing for USAF test target dataset.

We note that this USAF dataset was acquired during an earlier stage of the beamline development, leading to reduced usable HHG flux and to longer acquisition times than in the Abbe portrait datasets. All throughput evaluations in the main text refer to the later, optimised configuration used for the Abbe portrait datasets.

mPIE stage	Iterations	β_{obj}	β_{probe}	α_{obj}	α_{probe}	feedback	friction
1	10	0.3	0.02	0.9	0.9	0.3	0.7
2	100	0.3	0.25	0.9	0.9	0.3	0.7
OPR stage	Iterations	OPR modes	OPR subspace	β_{obj}	β_{probe}		
1	150	2	2	0.99	0.99		

Table S2. Hyperparameters used in the mPIE [7] and OPRP [12] reconstruction engines for the USAF test target datasets. Each row corresponds to one reconstruction stage with fixed parameters and the indicated number of iterations.

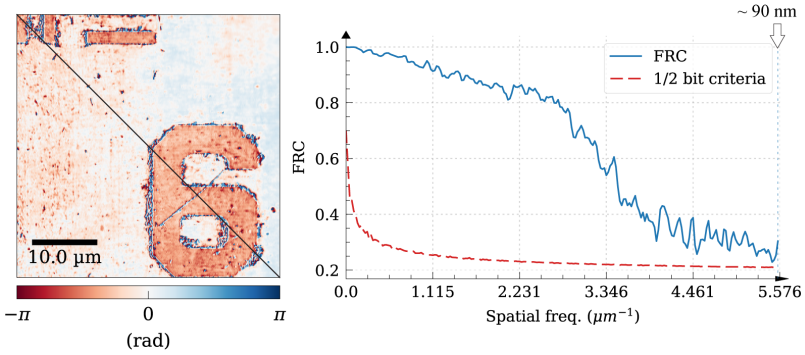

Fig. S6. Split-view comparison of the same region of interest (ROI) from two independent reconstructions (left) and the corresponding Fourier ring correlation (FRC) curve (right). The FRC remains above the 1/2-bit criterion [3] up to the highest sampled spatial frequency; the vertical line marks the corresponding spatial resolution of ∼ 90 nm.

B. Abbe portrait HDR

(a) Acquisition parameters	
Number of scan positions	255
Average step size	4 μm
Distance to detector z	43 mm
Wavelength	46.65 nm
Angle of incidence θ_i	45 °
Detector pixel size Δ_q	11 μm
Detector size N_q	2048×2048

(b) Timing breakdown (per position and total)	
Avg. dwell time per position	300 ms
Avg. readout time per frame	150 ms
Avg. saving time per position	160 ms
Exposure time per position	10 ms + 500 ms
Total exposure time	130 s
Total acquisition time	**∼5.4 min**

Table S3. Overview of acquisition parameters and timing for Abbe portrait HDR dataset.

mPIE Stage	Iterations	β_{obj}	β_{probe}	α_{obj}	α_{probe}	feedback	friction
1	2	0.3	0.05	0.9	0.9	0.3	0.7
2	300	0.3	0.25	0.9	0.9	0.3	0.7

Table S4. Hyperparameters used in the mPIE [7] reconstruction engine for the HDR Abbe portrait dataset. Each row corresponds to one reconstruction stage with fixed parameters and the indicated number of iterations.

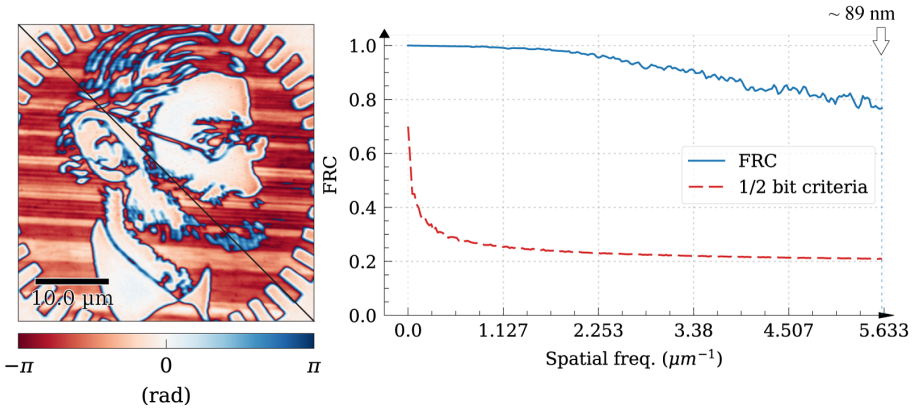

Fig. S7. Split-view comparison of the same region of interest (ROI) from two independent reconstructions (left) and the corresponding Fourier ring correlation (FRC) curve (right). The FRC remains above the 1/2-bit criterion [3] up to the highest sampled spatial frequency; the vertical line marks the corresponding spatial resolution of 89 nm.

C. Abbe portrait $s-$ and $p-$polarisation datasets

(a) Acquisition parameters	
Number of scan positions	255
Average step size	4 μm
Distance to detector z	43 mm
Wavelength	46.65 nm
Angle of incidence θ_i	45 °
Detector pixel size Δ_q	11 μm
Detector size N_q	2048×2048

(b) Timing breakdown (per position and total)	
Avg. dwell time per position	300 ms
Avg. readout time per frame	150 ms
Avg. saving time per position	80 ms
Exposure time	100 ms
Total exposure time	25.5 s
Total acquisition time	**∼2.4 min**

Table S5. Overview of acquisition parameters and timing for Abbe portrait $s-$ and $p-$polarisation datasets.

mPIE Stage	Iterations	β_{obj}	β_{probe}	α_{obj}	α_{probe}	feedback	friction
1	2	0.3	0.05	0.9	0.9	0.3	0.7
2	100	0.3	0.25	0.3	0.3	0.3	0.7
3	200	0.3	0.25	0.5	0.5	0.3	0.7

Table S6. Hyperparameters used in the mPIE [7] reconstruction engine for Abbe portrait $s-$ and $p-$polarisation datasets. Each row corresponds to one reconstruction stage with fixed parameters and the indicated number of iterations.

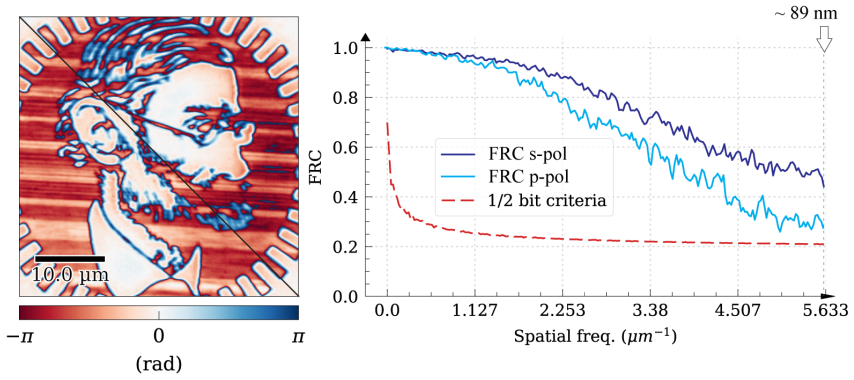

Fig. S8. Split-view comparison of the same ROI from two independent s-polarised reconstructions (left); the same ROI was used for the p-polarisation (not shown). Corresponding FRC curves for both polarisations, which remain above the 1/2-bit criterion [3] up to the highest spatial frequency. The p-polarised data exhibit a slightly lower FRC trend, consistent with their reduced signal-to-noise ratio. The vertical line marks the corresponding spatial resolution of 89 nm achieved in both polarisations.

D. Abbe portrait $s-$polarisation (low overlap) dataset

(a) Acquisition parameters	
Number of scan positions	55
Average step size	8.2 μm
Distance to detector z	43 mm
Wavelength	46.65 nm
Angle of incidence θ_i	45 °
Detector pixel size Δ_q	11 μm
Detector size N_q	2048×2048

(b) Timing breakdown (per position and total)	
Avg. dwell time per position	300 ms
Avg. readout time per frame	150 ms
Avg. saving time per position	80 ms
Exposure time	50 ms
Total exposure time	2.75 s
Total acquisition time	**∼0.5 min**

Table S7. Overview of acquisition parameters and timing for Abbe portrait $s-$polarisation (low overlap) dataset.

mPIE Stage	Iterations	β_{obj}	β_{probe}	α_{obj}	α_{probe}	feedback	friction
1	2	0.3	0.05	0.9	0.9	0.3	0.7
2	100	0.3	0.25	0.3	0.3	0.3	0.7
3	200	0.3	0.25	0.5	0.5	0.3	0.7

Table S8. Hyperparameters used in the mPIE [7] reconstruction engine for Abbe portrait $s-$polarisation (low overlap) dataset. Each row corresponds to one reconstruction stage with fixed parameters and the indicated number of iterations.

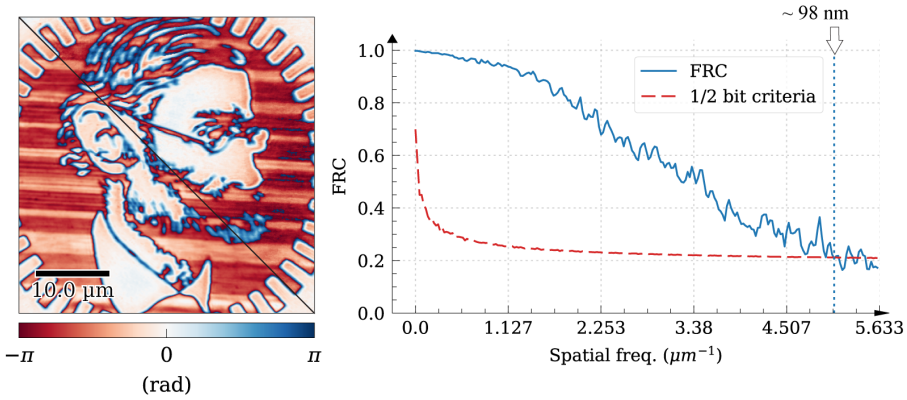

Fig. S9. Split-view comparison of the same region of interest (ROI) from two independent reconstructions (left) and the corresponding Fourier ring correlation (FRC) curve (right). The point where the FRC curve drops below the 1/2-bit criterion [3] marks the corresponding achieved spatial resolution of ∼ 98 nm.

4. THROUGHPUT DETAILS

Following the evaluated spatial resolution via the FRC and 1/2-bit criteria [3]. We evaluate the throughput of our reconstructions in terms of pixels per hour. Table S9 summarises these values that were plotted in the main text of the manuscript.

Configuration	*Pol.*	N	A_{rec}	T_{acq}	δ_x	*Throughput*
HDR, 94 % overlap	s	255	8100 μm^2	5.4 min	89 nm	11.4 Mpx h^{-1}
94 % overlap	s	255	8100 μm^2	2.7 min	89 nm	22.7 Mpx h^{-1}
94 % overlap	p	255	8100 μm^2	2.7 min	89 nm	22.7 Mpx h^{-1}
84 % overlap	s	55	8100 μm^2	0.5 min	98 nm	98.1 Mpx h^{-1}

Table S9. Experimental parameters and effective throughput for different EUV reflection ptychography configurations in this work. The configuration, polarisation state, number of scan positions, reconstructed area, total acquisition time T (including detector readout and stage overhead), achieved spatial resolution, and resulting throughput are listed.

5. LOCAL MATERIAL IDENTIFICATION

We can use the polarisation-resolved reconstructions to compare the material response of distinct regions locally. The first row in Fig. S10 shows a section of the complex-valued reconstructions, after this material-referencing step, for each polarisation state: the Abbe portrait is clearly resolved in both, with slightly reduced reconstruction quality in the p-polarisation reconstruction owing to its lower signal-to-noise ratio. From these phase-referenced s- and p-polarised reconstructions, we then computed the experimental complex reflection ratio ρ.

As described in Methods section in the main manuscript, the complex reflection ratio ρ isolates the polarisation-dependent reflectivity by suppressing the topography-induced phase contribution. Fig. S10 (c) shows a split view of the spatial distribution of ρ illustrating its amplitude $|\rho|$ and phase $\arg(\rho)$. On top of it, three markers were added to indicate the Si_3N_4 reference region used for the global phase/offset correction, and two regions of interest: inside and outside the FIB-milled area. The corresponding ρ values from the three marked regions of interest (ROIs), taken from pixels within a 15-pixel radius of each ROI centre, are plotted in the complex (Cartesian) plane in Fig. S10(d), where they form three well-separated clusters. For comparison, we overlay the calculated values of ρ for candidate materials (Si_3N_4, Ga, Ga_2O_3, and C; black diamonds). By construction, the centroid of the reference ROI cluster coincides with the Si_3N_4 point, since this region is used to define the complex referencing. The other two experimental clusters and centroids fall in the vicinity of the theoretical points for Ga-, Ga_2O_3-, and C-like responses, but do not coincide exactly with any single bulk material. Determining a plausible layered structure whose effective complex ratio ρ reproduces these cluster centroids is precisely the type of modelling task addressed in conventional ellipsometry; here, the substrate and plausible contamination species are known *a priori*. Although our single-angle approach does not uniquely constrain a solution for their absolute overlayer thickness, the observed separation in complex-ρ space is consistent with the presence of Ga-rich and carbonaceous surface layers.

The finite width of the clusters in the complex-ρ plane reflects uncertainty in both the amplitude ratio (radial direction) and the phase difference (tangential direction) between the polarisation-resolved reconstructions. Writing the complex ratio as

$$\rho = \frac{r_p}{r_s} = \left(\frac{|r_p|}{|r_s|}\right) \exp\left[i(\phi_p - \phi_s)\right],$$

we identify $|r_p|/|r_s|$ as the modulus of ρ (radial coordinate) and $\phi_p - \phi_s$ as its argument (angular coordinate), where $|r_{s,p}|$ and $\phi_{s,p}$ denote the amplitude and phase of the s- and p-polarised reflection coefficients, respectively. In particular, since

$$\arg(\rho) = \arg(r_p) - \arg(r_s) = \phi_p - \phi_s,$$

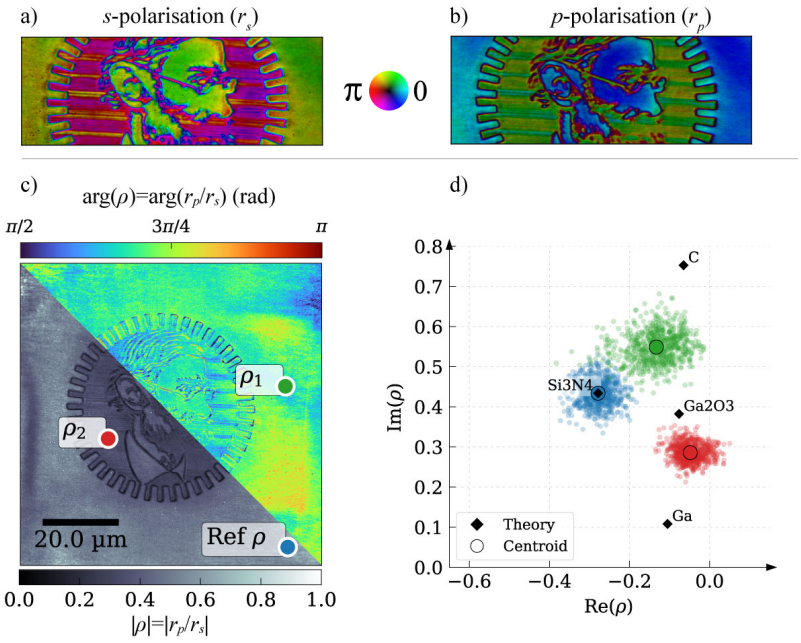

Fig. S10. Material identification from polarisation-resolved reconstructions. (a,b) Sections of the reconstructed field of view after the material-referencing step for each polarisation state. Hue encodes phase, and brightness encodes amplitude. (c) Split view of the amplitude and phase of the complex reflection ratio ρ, with markers indicating the reference-material region and two ROIs inside and outside the FIB-milled region. Each ROI is defined as the set of pixels within a 15-pixel radius of the marked centre. (d) Corresponding ρ values from the three ROIs plotted in the complex plane, $(\mathrm{Re}(\rho), \mathrm{Im}(\rho))$, revealing distinct signatures for the selected regions.

the phase repeatability limits in r_s and r_p propagate into an effective phase spread of the ratio,

$$\sigma_{\phi_\rho} \approx \sqrt{\sigma_{\phi_p}^2 + \sigma_{\phi_s}^2},$$

assuming uncorrelated phase uncertainties in the two reconstructions. Numerically, this gives a phase spread on the order of ~ 0.1 rad, consistent with the measured repeatability of ~ 70 mrad for s polarisation and an estimated ~ 80 mrad for p polarisation. An analogous argument applies qualitatively to the radial spread of the clusters: uncertainties in the amplitudes $|r_p|$ and $|r_s|$ propagate into a finite radial extent of the amplitude ratio $|r_p|/|r_s|$ in the complex-ρ plane, even though we do not quantify the amplitude repeatability separately here. We note that within-ROI heterogeneity and local variations in effective AOI could also influence the extent of these clusters.

We note that the bimodal structure of the ρ distribution does not rely on phase-referencing to a known material. Because ptychography recovers the complex response only up to an arbitrary global phase (and a relative complex offset between the two polarisations), omitting the reference shifts the entire ρ cloud to a different location in the complex plane; however, the relative separation and the two predominant modes remain. Referencing an area of known composition is therefore not required for discrimination, but it enables a physically meaningful alignment to theoretical ρ values and thereby guides the identification of likely neighbouring material species.

6. OPTICAL PATH DIFFERENCE ENCODES TOPOGRAPHY

In a scalar model of reflection, the reconstructed complex object for a given polarisation state, $\widetilde{O}_{\mathrm{pol}}(\mathbf{r})$, can be expressed as

$$\widetilde{O}_{\mathrm{pol}}(\mathbf{r}) = A(\mathbf{r})\, \exp\left[i\phi_{\mathrm{OPD}}(\mathbf{r})\right] \widetilde{r}_{\mathrm{pol}},$$

where amplitude variations due to illumination inhomogeneity and surface roughness are encoded in $A(\mathbf{r})$, phase variations due to surface height changes are contained in $\exp\left[i\phi_{\mathrm{OPD}}(\mathbf{r})\right]$, and the complex material response is described by $\widetilde{r}_{\mathrm{pol}}$. If we consider the object to be monolithic, $\widetilde{r}_{\mathrm{pol}}$ is constant over the field of view, and we can translate the phase into a height map via the geometrical relation

$$\phi_{\mathrm{OPD}}(\mathbf{r}) = \frac{2\pi}{\lambda}\left(-2h(\mathbf{r})\cos\theta_i\right), \tag{S1}$$

where λ is the wavelength and θ_i is the angle of incidence measured from the surface normal. The interpretation of this expression is illustrated in Fig. S11: the factor of 2 accounts for the round trip introduced by a height variation h, and the optical path difference is proportional to $\cos\theta_i$. The minus sign follows the convention that a downward step from the reference plane, corresponding to a negative h, increases the optical path length and thus results in a positive OPD. A more detailed derivation of Eq. (S1) can be found in standard optics textbooks [13].

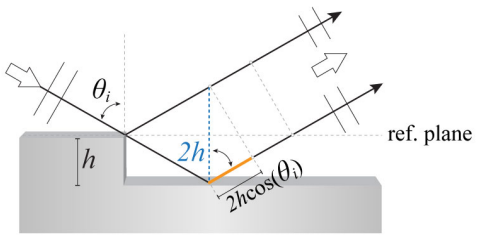

Fig. S11. Geometrical interpretation of the optical path difference (OPD) in reflection. A plane wave is incident on the sample at an angle θ_i measured from the surface normal. A local step of height $h(\mathbf{r})$ relative to the reference plane shifts the reflection point and introduces an additional optical path (orange) proportional to $2h(\mathbf{r})\cos\theta_i$.

The power of this geometrical phase relation comes from the high phase precision achievable with ptychography. The smallest phase change that ptychography can reliably detect determines the smallest resolvable height variation in the axial direction. For typical phase standard errors of $\sigma_\phi \lesssim 80$ mrad, the corresponding height sensitivity is

$$\Delta h = \frac{\lambda}{4\pi}\,\frac{\sigma_\phi}{\cos\theta_i} \approx \frac{\lambda}{100} \quad \text{for} \quad \sigma_\phi \sim 80\ \text{mrad},\ \theta_i = 45^\circ. \tag{S2}$$

This relation highlights two points. First, the axial height sensitivity can be far smaller than the wavelength, so Å-scale height changes are detectable even at EUV wavelengths. Second, because Δh grows as $1/\cos\theta_i$, very grazing incidence angles (e.g. $\theta_i \gtrsim 80^\circ$ when measured from the surface normal) actually degrade height sensitivity in this simple OPD picture. Operating in the Brewster-angle range therefore not only provides strong polarisation contrast for material identification, but also maintains an axial height sensitivity nearly two orders of magnitude smaller than the wavelength. We note, however, that the phase is measured modulo 2π, so the Δh relation strictly describes the local sensitivity of small phase variations. For structures with large height variations that produce multiple phase wraps, careful phase unwrapping is required to recover an unambiguous height map from ϕ_{OPD}.

7. STANDARD PHASE NOISE

The phase-difference noise between two independent reconstructions provides an estimate of the phase precision and, through the OPD relation, of the height sensitivity. For our largest field of view of 90 µm × 90 µm, we obtain a standard deviation of the phase differences of $\sigma_\phi \approx 74$ mrad, corresponding to a height noise level of ~ 4 Å. For the smallest ROI, the phase standard deviation reduces to $\sigma_\phi \approx 35.8$ mrad, corresponding to a height noise level of ~ 2 Å.

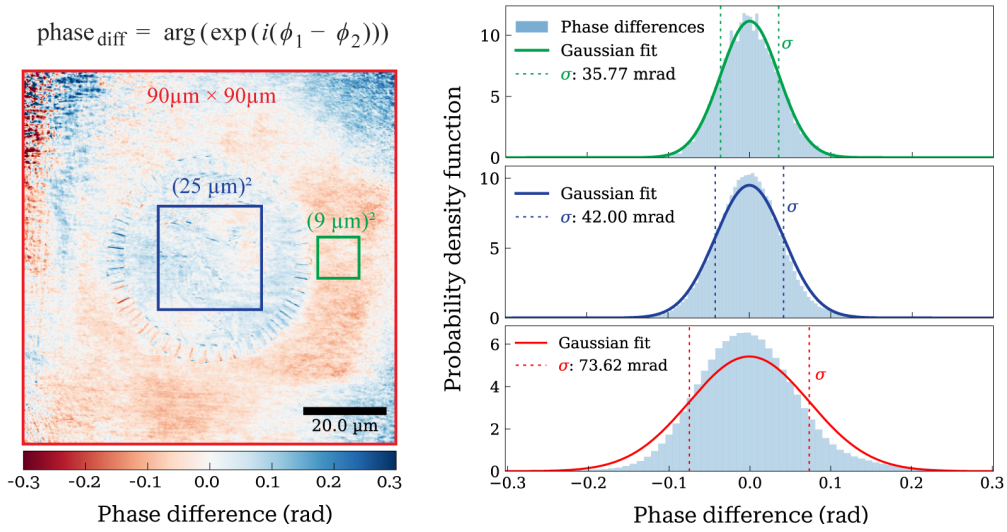

Fig. S12. Estimation of the phase-difference noise between two independent reconstructions. Wrapped phase-difference map with marked ROIs indicated (left). Histograms of the phase differences within each ROI, approximating the corresponding probability density functions (PDFs), together with the fitted Gaussians and their standard deviations σ (right).

8. MATERIAL PARAMETERS FOR REFLECTIVITY CURVES

Standard optical-constant databases (e.g., `xraydb` [14]) are truncated at low photon energies (below 30 eV). Nevertheless, the tabulated atomic scattering factors f_1 and f_2 can be used to compute the δ, β parameters for the expected contaminants using the standard formalism [15]:

$$\delta + i\beta = (r_e \lambda^2 / 2\pi) \sum_j n_j \, [Z_j + f_{1,j} + i f_{2,j}].$$

We assess the validity of this procedure by verifying that the resulting δ, β follow the expected trends at higher photon energies (see Fig. S13, and summarise these parameters in Table S10.

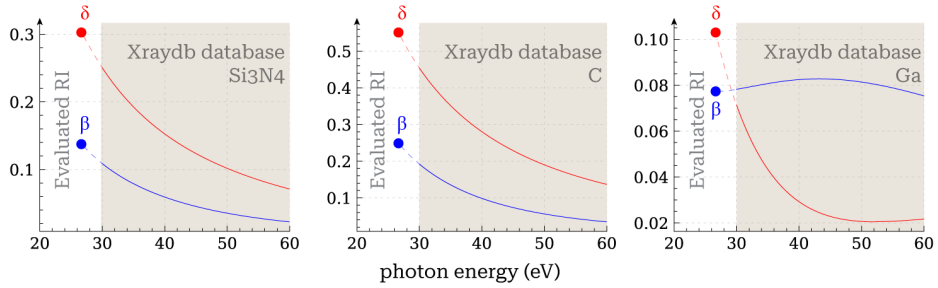

Fig. S13. RI values extrapolation below 30 eV based on the scattering factors of Table S10 and Ref.[15]. The shaded area corresponds to the `xraydb` database [14].

REFERENCES

1. D. F. Gardner, B. Zhang, M. D. Seaberg, *et al.*, "High numerical aperture reflection mode coherent diffraction microscopy using off-axis apertured illumination," Opt. express **20**, 19050–19059 (2012).
2. H. Lu, M. Odstrčil, C. Pooley, *et al.*, "Characterisation of engineered defects in extreme ultraviolet mirror substrates using lab-scale extreme ultraviolet reflection ptychography," Ultramicroscopy **249**, 113720 (2023).
3. M. Van Heel and M. Schatz, "Fourier shell correlation threshold criteria," J. structural biology **151**, 250–262 (2005).

(a) Atomic scattering factors.

Element	f_1	f_2
Si	−10.413	0.156
N	−3.964	2.483
Ga	−28.919	1.563
O	−5.30025	3.41518
C	−2.78365	1.4519

(b) Material densities and optical constants.

Material	ρ (g cm^{-3})	δ	β
Si_3N_4	3.17	0.303	0.137
Ga	5.90	0.103	0.077
Ga_2O_3	5.91	0.225	0.245
C	3.52	0.551	0.249

Table S10. Atomic scattering factors and material optical constants at $E = 26.65$ eV. The refractive $n = 1 - \delta + i\beta$ is computed following Ref.[15]. Scattering factors are taken from the `xraydb` database [14].

4. D. Zhu, X. Wang, Q. Fang, *et al.*, "Pushing the resolution limit by correcting the ewald sphere effect in single-particle cryo-em reconstructions," Nat. communications **9**, 1552 (2018).
5. A. M. Maiden, M. J. Humphry, F. Zhang, and J. M. Rodenburg, "Superresolution imaging via ptychography," J. Opt. Soc. Am. A **28**, 604–612 (2011).
6. L. Loetgering, M. Du, D. Boonzajer Flaes, *et al.*, "Ptylab. m/py/jl: a cross-platform, open-source inverse modeling toolbox for conventional and fourier ptychography," Opt. Express **31**, 13763–13797 (2023).
7. A. Maiden, D. Johnson, and P. Li, "Further improvements to the ptychographical iterative engine," Optica **4**, 736–745 (2017).
8. P. Thibault and A. Menzel, "Reconstructing state mixtures from diffraction measurements," Nature **494**, 68–71 (2013).
9. P. Li, "Investigations and improvements in ptychographic imaging," Ph.D. thesis, University of Sheffield (2016).
10. R. Röhrich, A. F. Koenderink, S. Witte, and L. Loetgering, "Spatial coherence control and analysis via micromirror-based mixed-state ptychography," New J. Phys. **23**, 053016 (2021).
11. C. Liu, W. Eschen, D. S. Penagos Molina, *et al.*, "Purity-based self-calibration in ptychography," Opt. Lett. **50**, 1581–1584 (2025).
12. M. Odstrcil, P. Baksh, S. Boden, *et al.*, "Ptychographic coherent diffractive imaging with orthogonal probe relaxation," Opt. express **24**, 8360–8369 (2016).
13. D. S. Goodman, "General principles of geometric optics," Hand Book Opt. **1**, 68–69 (1996).
14. M. Newville *et al.*, "Xraydb: X-ray reference data in sqlite," https://github.com/xraypy/XrayDB (2023). Python interface accessed via the `xraydb` package.
15. C. Jacobsen, *X-ray Microscopy* (Cambridge University Press, 2019).